

The versatile polyhedral elements of Cosserat continuum theory based on SBFEM and its application

Xiupeng Nie^{a,b}, Degao Zou^{a,b}, Kai Chen^{a,b,*}, Jingmao Liu^{a,b}, Xianjing Kong^{a,b}, Yongqian Qu^{a,b}

^a The State Key Laboratory of Coastal and Offshore Engineering, Dalian University of Technology, Dalian, Liaoning 116024, China

^b School of Hydraulic Engineering, Dalian University of Technology, Dalian, Liaoning 116024, China

ARTICLE INFO

Keywords:

Cosserat continuum
Micro-structure analysis
Stress concentration
Internal length scale
Three-dimensional
The polyhedral scale boundary finite element method

ABSTRACT

The Cosserat continuum offers high accuracy in micro-structure analysis and stress concentration simulation due to its consideration of mechanical factors such as coupled stress and internal length scale. However, existing methods are mainly developed based on the isoparametric conventional continuum framework, with relatively simple element shapes and weak adaptability to complex geometries. Therefore, this paper proposes an improved Cosserat continuum theory based on the three-dimensional (3D) polyhedral scale boundary finite element method (PSBFEM). The main work is as follows: (1) The Cosserat continuum theory formula is deduced within the SBFEM framework by integrating a polygon mean-value shape function; (2) The analytical accuracy of the proposed method is examined through classical micro-structure test examples; (3) An efficient octree algorithm is introduced to evaluate the comprehensive performance of the proposed method for the analysis of complex structures, and the selection and impact of the internal length scale are discussed. The results indicate that the proposed method incorporates the good performance of SBFEM and the Cosserat continuum, and its accuracy can approach the traditional quadratic Cosserat continuum elements; The stress concentration problem can be effectively addressed, leading to a more accurate representation of structural stress characteristics. Additionally, complex polyhedral elements can be directly calculated, and the element library of traditional Cosserat theory has been greatly expanded.

1. Introduction

In geotechnical engineering, finite element numerical simulation is typically based on classical continuum mechanics theory. However, when it comes to certain micro-structure problems, such as the size effect of materials and the stress concentration problem, the application of classical continuum theory will be challenged, and its applicability will be limited. Therefore, it is necessary to replace the classical continuum theory to better address specific problems mentioned above in numerical research.

Currently, a batch of methods is available to address the limitations of classical continuum theory in numerical simulation. Among these, the micro-polar (Cosserat) continuum theory has been recognized to be a very novel alternative due to its convenient and straightforward program execution [1,2]. The Cosserat continuum theory was proposed by Cosserat brothers [3] in the early 20th century and has been considered a robust and superior approach to solving micro-structure problems. The Cosserat continuum assumes that the microelement of materials is a

representative element with a specific size, capable of reflecting the micro-structure of the material. In contrast, the classical continuum theory considers the microelement in materials as an infinitesimal mathematical point [4]. This theory also incorporates the additional rotational degrees of freedom in addition to translational degrees of freedom in classical continuum theory. Another characteristic of this theory is the incorporation of a material parameter called the internal length scale in the constitutive formulation. Furthermore, the micro-curvatures' spatial derivatives of the rotational degree of freedom, and the energetically conjugate coupled stresses to the micro-curvatures are also introduced [5–7].

Since the concept of the Cosserat continuum was proposed, the corresponding research has been carried out extensively. In the 1960s, Toupin [8] and Mindlin [9] conducted preliminary research on this theory, laying the mathematical foundation for its promotion. Borst [10] first introduced the Cosserat continuum theory into the field of finite element method (FEM) and implemented it with finite element code. Cosserat theory was formally applied in the field of geotechnical

* Corresponding author at: The State Key Laboratory of Coastal and Offshore Engineering, Dalian University of Technology, Dalian, Liaoning 116024, China.
E-mail address: chenkai@dlut.edu.cn (K. Chen).

engineering in the late 1980s, many researchers are aware of the advantages of this theory in tackling specific problems in geotechnical engineering and have dedicated themselves to corresponding research to advance the development of this theory [11–15].

The aforementioned research on the Cosserat continuum mainly focuses on two-dimensional (2D) plane strain problems, even though the actual engineering problems are commonly three-dimensional (3D). The main reason for this deficiency is that 3D Cosserat requires more complex algorithms and more stress and strain components, making it difficult to implement it numerically. So far, Riahi and Curran [16] have applied the Cosserat FEM theory to analyze the phenomena of small deformation and strain localization in 3D structures. Tang and Hu [14] studied the size effects in 3D cantilever beams, the mesh-independent problem with strain softening behavior based on Cosserat continuum theory.

In 3D analysis, the conventional element types utilized in FEM include hexahedrons, tetrahedrons, wedges, and pyramids [17,18]. These elements could be clumsy and incompetent when discretizing structures with complicated geometric shapes. In comparison, discretization using the octree-based adaptive refinement algorithm has the advantage of automatic mesh generation and excellent geometric adaptability, particularly for numerical analysis problems involving complex geometric shapes [19]. During the implementation process, numerous hanging nodes exist in the mesh between different-sized elements, hence presenting a significant challenge for traditional FEM. Several numerical methods have been developed to eliminate the limitations in the polyhedral elements of finite element meshes [20–22]. Among these methods, the scaled boundary element method (SBFEM) has garnered increased attention from researchers in recent years [23–26].

SBFEM is a semi-analytical numerical method first developed by Wolf and Song [20], it combines some advantages of FEM and the boundary element method (BEM). After recent developments, the SBFEM theory has been systematically established as a mature framework by Song [27–30], thereby offering readers a broader range of theoretical knowledge in multiple fields. In SBFEM, only the discretization of element boundaries is required, which provides the benefit of reducing spatial dimensions. As a result, the boundary surfaces with hanging nodes can be treated as polygonal elements without any extra effort. Secondly, the solutions of the SBFEM are numerical in the circumferential direction and analytical in the radial direction, making it superior in terms of computational accuracy. Thirdly, SBFEM offers flexibility and versatility in numerous engineering applications. These superiorities have made SBFEM a promising numerical method and have been utilized to solve various engineering problems. Liu et al. [31–34] developed a novel isogeometric SBFEM for shells and bending and vibration analyses of structures. Du et al. [35,36] utilized SBFEM to tackle the challenges of static and dynamic crack initiation and propagation, offering a more precise depiction of local cracking damage zones. Zhang et al. [37–40] proposed a flexible structural dynamic analysis method based on SBFEM and achieved engineering applicability. Guo et al. [41, 42] applied SBFEM to the topology optimization problem, resulting in satisfactory improvements in computational efficiency and simplification of the implementation process. Researchers have also conducted SBFEM research in various fields, including dam numerical simulation [18,23], 2D Cosserat continuum analysis [43], adaptive mesh refinement analysis [44,45], structural damage analysis [46–49], the transient analysis of elastic wave propagation [50], and the direct numerical analysis on point-cloud models [51]. It is noteworthy that the combination of Cosserat continuum theory and SBFEM (Cosserat SBFEM) has only been studied preliminarily in 2D problems. To address this gap, this study proposes a research on 3D Cosserat SBFEM for structural analysis.

In this paper, an improved Cosserat continuum theory formula is deduced based on the 3D PSBFEM by introducing the polygon mean-value shape function. Then, the proposed method is verified through two classical micro-structure test examples. Finally, the octree algorithm

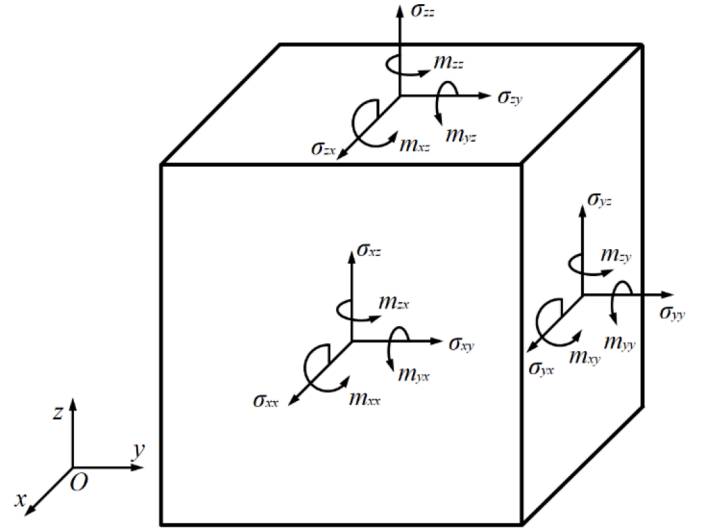


Fig. 1. Stress and couple stress in 3D Cosserat continuum.

is applied to investigate the universality of the proposed method in 3D complex structures. Some inherent advantages of SBFEM and Cosserat theory can be naturally inherited. The proposed method offers excellent accuracy in micro-structure analysis comparable to that of isoparametric quadratic Cosserat continuum elements. Additionally, it provides a more realistic representation of the stress concentration problem. Moreover, the applicability of analyzing complex structures is well possessed.

The remainder of this paper is organized as follows: The 3D Cosserat continuum theory is introduced in Section 2. A theoretical derivation of 3D SBFEM for Cosserat continuum is described in Section 3. Section 4 presents the analytical accuracy and applicability of the proposed method. Finally, the main findings of this study are summarized in Section 5.

2. Summary of 3D Cosserat continuum

In addition to three translational degrees of freedom (u_x, u_y, u_z), three independent rotational degrees of freedom ($\omega_x, \omega_y, \omega_z$) are added to each material point of 3D Cosserat continuum material, that is, rotation is a rigid item that is attached to the material point and independent of three translational degrees of freedom. Therefore, in the 3D Cosserat continuum, each material point has six independent degrees of freedom, namely

$$u = [u_x \quad u_y \quad u_z \quad \omega_x \quad \omega_y \quad \omega_z]^T \quad (2.1)$$

where, the subscript of the translational degrees-of-freedom represents the direction of the displacement, and the subscript of the rotational degrees-of-freedom represents the rotation axis. Besides, the strain and stress components in the Cosserat continuum consider the microscopic curvature and moment. Therefore, the number of mechanical variables of 3D elements increases from seven to eighteen. This includes nine conventional stresses and nine couple stresses, which can be written as:

$$\varepsilon = [\varepsilon_{xx} \quad \varepsilon_{yy} \quad \varepsilon_{zz} \quad \varepsilon_{xy} \quad \varepsilon_{yx} \quad \varepsilon_{yz} \quad \varepsilon_{zy} \quad \varepsilon_{zx} \quad \varepsilon_{xz} \quad \kappa_{xx}l_t \quad \kappa_{yy}l_t \quad \kappa_{zz}l_t \quad \kappa_{xy}l_b \quad \kappa_{yx}l_b \quad \kappa_{yz}l_b \quad \kappa_{zy}l_b \quad \kappa_{zx}l_b \quad \kappa_{xz}l_b]^T \quad (2.2)$$

$$\sigma = \left[\sigma_{xx} \quad \sigma_{yy} \quad \sigma_{zz} \quad \sigma_{xy} \quad \sigma_{yx} \quad \sigma_{yz} \quad \sigma_{zy} \quad \sigma_{zx} \quad \sigma_{xz} \quad \frac{m_{xx}}{l_t} \quad \frac{m_{yy}}{l_t} \quad \frac{m_{zz}}{l_t} \quad \frac{m_{xy}}{l_b} \quad \frac{m_{yx}}{l_b} \quad \frac{m_{yz}}{l_b} \quad \frac{m_{zy}}{l_b} \quad \frac{m_{zx}}{l_b} \quad \frac{m_{xz}}{l_b} \right]^T \quad (2.3)$$

in which κ_{xx}, κ_{yy} and κ_{zz} are torsional microcurvature components, $\kappa_{xy}, \kappa_{yx}, \kappa_{yz}, \kappa_{zy}, \kappa_{zx}$ and κ_{xz} are bending microcurvature components. l_t and l_b are defined as the internal length scales for torsion and bending,

respectively [14]. m_{xx} , m_{yy} , and m_{zz} are the torsion couple-stress components conjugate to the torsional curvatures, and m_{xy} , m_{xz} , m_{yx} , m_{yz} , m_{zx} , and m_{zy} are the bending couple-stress components conjugate to the bending curvatures. The stress and couple stress states of the Cosserat continuum in the 3D case are shown in Fig. 1.

The relationship between the displacement components and strain components in Cosserat theory can be written as

$$\varepsilon = Lu \quad (2.4)$$

where, the differential operator matrix L is written as

$$L = \begin{bmatrix} L_1 \\ L_2 \end{bmatrix} \quad (2.5)$$

where,

$$L_1 = \begin{bmatrix} \frac{\partial}{\partial x} & 0 & 0 & 0 & 0 & 0 \\ 0 & \frac{\partial}{\partial y} & 0 & 0 & 0 & 0 \\ 0 & 0 & \frac{\partial}{\partial z} & 0 & 0 & 0 \\ 0 & \frac{\partial}{\partial x} & 0 & 0 & 0 & -1 \\ \frac{\partial}{\partial y} & 0 & 0 & 0 & 0 & 1 \\ 0 & 0 & \frac{\partial}{\partial y} & -1 & 0 & 0 \\ 0 & \frac{\partial}{\partial z} & 0 & 1 & 0 & 0 \\ \frac{\partial}{\partial z} & 0 & 0 & 0 & -1 & 0 \\ 0 & 0 & \frac{\partial}{\partial x} & 0 & 1 & 0 \end{bmatrix}, \quad L_2 = \begin{bmatrix} 0 & 0 & 0 & l_r \frac{\partial}{\partial x} & 0 & 0 \\ 0 & 0 & 0 & 0 & l_r \frac{\partial}{\partial y} & 0 \\ 0 & 0 & 0 & 0 & 0 & l_r \frac{\partial}{\partial z} \\ 0 & 0 & 0 & l_b \frac{\partial}{\partial y} & 0 & 0 \\ 0 & 0 & 0 & l_b \frac{\partial}{\partial z} & 0 & 0 \\ 0 & 0 & 0 & 0 & l_b \frac{\partial}{\partial x} & 0 \\ 0 & 0 & 0 & 0 & l_b \frac{\partial}{\partial z} & 0 \\ 0 & 0 & 0 & 0 & 0 & l_b \frac{\partial}{\partial x} \\ 0 & 0 & 0 & 0 & 0 & l_b \frac{\partial}{\partial y} \end{bmatrix} \quad (2.6)$$

The corresponding linear elastic stress-strain constitutive relationship is

$$\sigma = D_e \varepsilon \quad (2.7)$$

In Eq. (2.7), D_e is the isotropic elastic matrix and it can be expressed as

$$D_e = \begin{bmatrix} D_u & 0 \\ 0 & D_\omega \end{bmatrix} \quad (2.8)$$

in which

$$D_u = \begin{bmatrix} \lambda+2G & \lambda & \lambda & 0 & 0 & 0 & 0 & 0 & 0 & 0 \\ \lambda & \lambda+2G & \lambda & 0 & 0 & 0 & 0 & 0 & 0 & 0 \\ \lambda & \lambda & \lambda+2G & 0 & 0 & 0 & 0 & 0 & 0 & 0 \\ 0 & 0 & 0 & G+G_c & G-G_c & 0 & 0 & 0 & 0 & 0 \\ 0 & 0 & 0 & G-G_c & G+G_c & 0 & 0 & 0 & 0 & 0 \\ 0 & 0 & 0 & 0 & 0 & G+G_c & G-G_c & 0 & 0 & 0 \\ 0 & 0 & 0 & 0 & 0 & G-G_c & G+G_c & 0 & 0 & 0 \\ 0 & 0 & 0 & 0 & 0 & 0 & 0 & G+G_c & G-G_c & 0 \\ 0 & 0 & 0 & 0 & 0 & 0 & 0 & G-G_c & G+G_c & 0 \end{bmatrix} \quad (2.9)$$

$$D_\omega = \begin{bmatrix} 2G & 0 & 0 & 0 & 0 & 0 & 0 & 0 & 0 & 0 \\ 0 & 2G & 0 & 0 & 0 & 0 & 0 & 0 & 0 & 0 \\ 0 & 0 & 2G & 0 & 0 & 0 & 0 & 0 & 0 & 0 \\ 0 & 0 & 0 & 2G & 0 & 0 & 0 & 0 & 0 & 0 \\ 0 & 0 & 0 & 0 & 2G & 0 & 0 & 0 & 0 & 0 \\ 0 & 0 & 0 & 0 & 0 & 2G & 0 & 0 & 0 & 0 \\ 0 & 0 & 0 & 0 & 0 & 0 & 2G & 0 & 0 & 0 \\ 0 & 0 & 0 & 0 & 0 & 0 & 0 & 2G & 0 & 0 \\ 0 & 0 & 0 & 0 & 0 & 0 & 0 & 0 & 2G & 0 \end{bmatrix} \quad (2.10)$$

where, $\lambda=2G\nu/(1-2\nu)$ is the Lamé's constant, G and ν are the shear modulus and Poisson's ratio, and G_c is the Cosserat shear modulus.

Based on the above analysis, the static equilibrium equation of a 3D elastic Cosserat medium can be obtained as

$$L^T \sigma + f = 0 \quad (2.11)$$

in which f is the external force matrix.

3. 3D SBFEM theory for Cosserat continuum

3.1. 3D coordinate transformation

In the context of SBFEM, the 3D domain and its boundary can be discretized into an arbitrary n -faced polyhedron, as illustrated in Fig. 2. A scaling center, denoted as O , is introduced inside the domain, and any point on the boundary of the polyhedron is directly visible (see Fig. 2). As in BEM, discretization is only performed on the 2D surface elements of the boundary, as long as the shape functions of the n -sided surface element exist.

A hexagonal surface element on the boundary of the polyhedron in Fig. 2 is selected as a representative to illustrate the discretization scheme. The corresponding parent element of the surface element is also shown in Fig. 2. The hexagonal surface element and the scaling center point together form a conical subdomain. The scaled boundary coordinate system (ξ, η, ζ) is introduced, in which the boundary of the subdomain is scaled by the dimensionless radial coordinate ξ . It equals zero at the scaling center and unity on the boundary surface. For the surface element, the domain is interpolated using the polygonal shape function $N(\eta, \zeta)$ in the local coordinates. Therefore, an arbitrary point in Cartesian coordinates (x, y, z) can be transformed to the local scaled boundary coordinates (ξ, η, ζ) using the transformation formulation

$$\begin{aligned} x(\xi, \eta, \zeta) &= x_0 + \xi N(\eta, \zeta) x_b \\ y(\xi, \eta, \zeta) &= y_0 + \xi N(\eta, \zeta) y_b \\ z(\xi, \eta, \zeta) &= z_0 + \xi N(\eta, \zeta) z_b \end{aligned} \quad (3.1)$$

where, (x_b, y_b, z_b) are the coordinates of the nodes on the boundary, and (x_0, y_0, z_0) are the coordinates of the scaling center point.

The displacement solution of SBFEM within each subdomain is approximated as

$$u(\xi, \eta, \zeta) = N_u(\eta, \zeta) u(\xi) \quad (3.2)$$

where, $u(\xi)$ is the displacement along the radial lines.

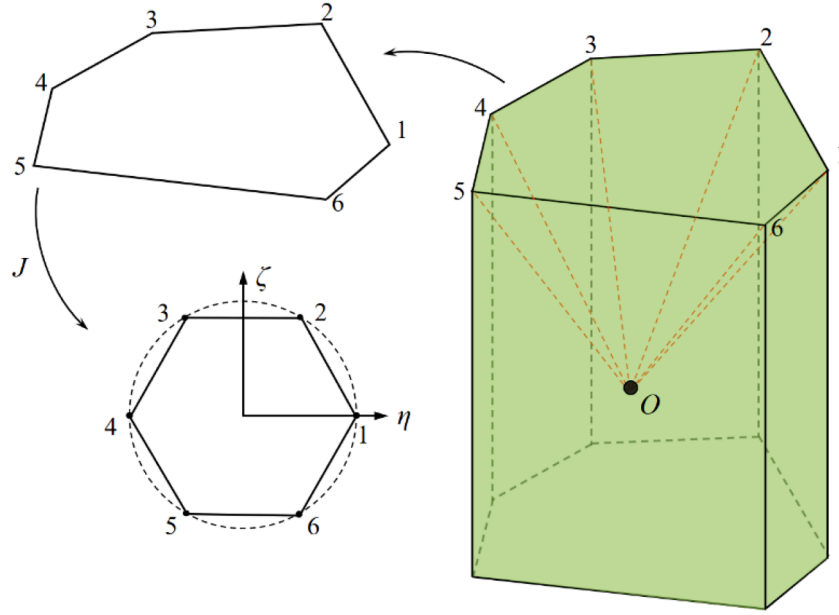


Fig. 2. The isoparametric mapping of a hexagonal element.

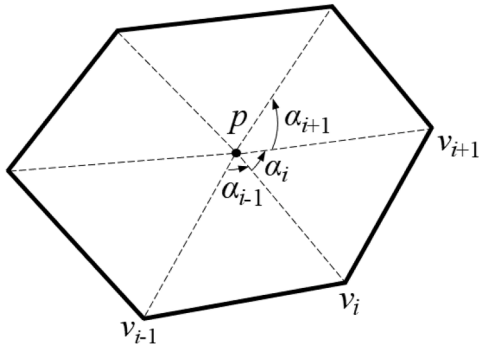


Fig. 3. Mean-value coordinates of polygon.

3.2. Polygonal surface shape function

To ensure the computational accuracy of polyhedral elements for SBFEM, the polygonal shape function for boundary surface interpolation is crucial. The shape functions for a polygon are generally expressed in the form of a rational polynomial due to its high-order approximation in numerical analysis [52]. Among these, the mean-value shape function receives more attention due to its simplicity and computational advantages [19], thus the mean-value shape function is applied in this study. According to the description in Floater et al. [53], for a point p in the n -polygon domain, the corresponding shape function $N_i(x)$ is represented by the non-negative weight function $w_i(x)$ and is expressed in the following form

$$N_i(x) = \frac{w_i(x)}{\sum_{j=1}^n w_j(x)} \quad (3.3)$$

$$w_i(x) = \frac{\tan(\alpha_{i-1}/2) + \tan(\alpha_i/2)}{\|x - x_i\|} \quad (3.4)$$

$$\tan(\alpha_i/2) = \frac{\sin \alpha_i}{1 + \cos \alpha_i} \quad (3.5)$$

where, n is the number of edges, α_i is the angle of $v_i p v_{i+1}$, and $\|x - x_i\|$ is the Euclidean distance between p and v_i , which are illustrated in Fig. 3.

Notably, the mean-value shape functions are represented in the

physical coordinate system. In this study, a conforming approximation technique of polygons for the mean-value shape function is adopted to align it with the local coordinate system in SBFEM theory. To be specific, polygons are standardized using an isoparametric mapping function λ , which transforms them into a canonical element. Schematic diagrams of n -sided canonical elements are shown in Fig. 4. The mapping process of a typical hexagonal element can be achieved through the Jacobian matrix J , as shown in Fig. 5, the details of the Jacobian matrix J are presented in Section 3.3. All nodes are located on the same circumscribed circle, and the geometric center of the canonical element is located at the center of the circumscribed circle. The node coordinates of an n -sided canonical element are obtained as $(\cos(2\pi/n), \sin(2\pi/n))$, $(\cos(4\pi/n), \sin(4\pi/n))$, ..., and $(1, 0)$. Then the shape function of the canonical element in local coordinates is naturally obtained.

3.3. SBFEM formulation with Cosserat theory

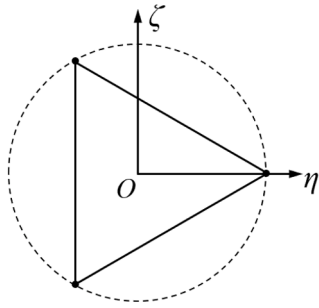
Combined with Cosserat theory, the relevant formulation of 3D Cosserat SBFEM can be deduced. In the 3D case, derivatives in the scaled boundary coordinate system can be related to derivatives in the Cartesian coordinate system through the Jacobian matrix J .

$$\begin{bmatrix} \frac{\partial}{\partial \xi} \\ \frac{1}{\xi} \frac{\partial}{\partial \eta} \\ \frac{1}{\xi} \frac{\partial}{\partial \zeta} \end{bmatrix} = J \cdot \begin{bmatrix} \frac{\partial}{\partial x} \\ \frac{\partial}{\partial y} \\ \frac{\partial}{\partial z} \end{bmatrix}, J = \begin{bmatrix} x(\eta, \zeta) & y(\eta, \zeta) & z(\eta, \zeta) \\ x(\eta, \zeta)_{,\eta} & y(\eta, \zeta)_{,\eta} & z(\eta, \zeta)_{,\eta} \\ x(\eta, \zeta)_{,\zeta} & y(\eta, \zeta)_{,\zeta} & z(\eta, \zeta)_{,\zeta} \end{bmatrix} \quad (3.6)$$

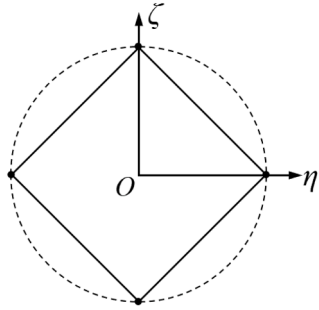
$$\begin{bmatrix} \frac{\partial}{\partial x} \\ \frac{\partial}{\partial y} \\ \frac{\partial}{\partial z} \end{bmatrix} = J^{-1} \cdot \begin{bmatrix} \frac{\partial}{\partial \xi} \\ \frac{1}{\xi} \frac{\partial}{\partial \eta} \\ \frac{1}{\xi} \frac{\partial}{\partial \zeta} \end{bmatrix} = \begin{bmatrix} A_{11} & A_{12} & A_{13} \\ A_{21} & A_{22} & A_{23} \\ A_{31} & A_{32} & A_{33} \end{bmatrix} \cdot \begin{bmatrix} \frac{\partial}{\partial \xi} \\ \frac{1}{\xi} \frac{\partial}{\partial \eta} \\ \frac{1}{\xi} \frac{\partial}{\partial \zeta} \end{bmatrix} \quad (3.7)$$

in which

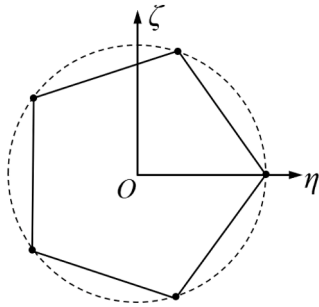
$$\begin{aligned} A_{11} &= y_{,\eta} z_{,\zeta} - y_{,\zeta} z_{,\eta}, & A_{12} &= y_{,\zeta} z - y_{,\eta} z_{,\zeta}, & A_{13} &= y_{,\eta} z_{,\eta} - y_{,\eta} z \\ A_{21} &= -x_{,\eta} z_{,\zeta} + x_{,\zeta} z_{,\eta}, & A_{22} &= x_{,\zeta} z - x_{,\eta} z_{,\zeta}, & A_{23} &= x_{,\eta} z - x_{,\eta} z_{,\eta} \\ A_{31} &= x_{,\eta} y_{,\zeta} - x_{,\zeta} y_{,\eta}, & A_{32} &= x_{,\zeta} y - x_{,\eta} y_{,\zeta}, & A_{33} &= x_{,\eta} y_{,\eta} - x_{,\eta} y \end{aligned} \quad (3.8)$$



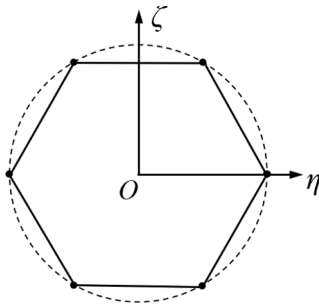
(a) triangular element



(b) quadrilateral element



(c) pentagonal element



(d) hexagonal element

Fig. 4. Canonical elements of n-polygon.

By substituting Eq. (3.7) into Eq. (2.5), the differential operator matrix L for 3D Cosserat SBFEM theory can be derived as:

$$L = b_1 \frac{\partial}{\partial \xi} + \frac{1}{\xi} \left(b_2 \frac{\partial}{\partial \eta} + b_3 \frac{\partial}{\partial \zeta} \right) + b_4 \quad (3.9)$$

in which

$$b_1 = \begin{bmatrix} b_{11} \\ b_{12} \end{bmatrix}, b_2 = \begin{bmatrix} b_{21} \\ b_{22} \end{bmatrix}, b_3 = \begin{bmatrix} b_{31} \\ b_{32} \end{bmatrix}, b_4 = \begin{bmatrix} b_{41} \\ b_{42} \end{bmatrix} \quad (3.10)$$

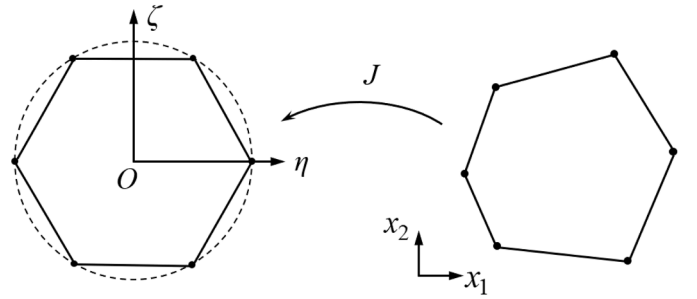


Fig. 5. The isoparametric mapping of a hexagonal element.

$$b_{i1}^T = \begin{bmatrix} A_{1i} & 0 & 0 & 0 & A_{2i} & 0 & 0 & A_{3i} & 0 & 0 \\ 0 & A_{2i} & 0 & A_{1i} & 0 & 0 & A_{3i} & 0 & 0 & 0 \\ 0 & 0 & A_{3i} & 0 & 0 & A_{2i} & 0 & 0 & A_{1i} & 0 \\ 0 & 0 & 0 & 0 & 0 & 0 & 0 & 0 & 0 & 0 \\ 0 & 0 & 0 & 0 & 0 & 0 & 0 & 0 & 0 & 0 \\ 0 & 0 & 0 & 0 & 0 & 0 & 0 & 0 & 0 & 0 \end{bmatrix}, (i=1 \sim 3) \quad (3.11)$$

$$b_{i2}^T = \begin{bmatrix} 0 & 0 & 0 & 0 & 0 & 0 & 0 & 0 & 0 & 0 \\ 0 & 0 & 0 & 0 & 0 & 0 & 0 & 0 & 0 & 0 \\ 0 & 0 & 0 & 0 & 0 & 0 & 0 & 0 & 0 & 0 \\ l_i A_{1i} & 0 & 0 & l_b A_{2i} & l_b A_{3i} & 0 & 0 & 0 & 0 & 0 \\ 0 & l_i A_{2i} & 0 & 0 & 0 & l_b A_{1i} & l_b A_{3i} & 0 & 0 & 0 \\ 0 & 0 & l_i A_{3i} & 0 & 0 & 0 & 0 & l_b A_{1i} & l_b A_{2i} & 0 \end{bmatrix}, (i=1 \sim 3) \quad (3.12)$$

$$b_{41}^T = \begin{bmatrix} 0 & 0 & 0 & 0 & 0 & 0 & 0 & 0 & 0 & 0 \\ 0 & 0 & 0 & 0 & 0 & 0 & 0 & 0 & 0 & 0 \\ 0 & 0 & 0 & 0 & 0 & 0 & 0 & 0 & 0 & 0 \\ 0 & 0 & 0 & 0 & 0 & -1 & 1 & 0 & 0 & 0 \\ 0 & 0 & 0 & 0 & 0 & 0 & 0 & -1 & 1 & 0 \\ 0 & 0 & 0 & -1 & 1 & 0 & 0 & 0 & 0 & 0 \end{bmatrix}, b_{42}^T = [0]_{6 \times 9} \quad (3.13)$$

By substituting Eqs. (3.9)–(3.13) into Eq. (2.4), the expression of the strain matrix is expressed as

$$\varepsilon = Lu = B_1^C u(\xi)_{,\xi} + \frac{1}{\xi} B_2^C u(\xi) + B_3^C u(\xi) \quad (3.14)$$

in which

$$\begin{aligned} B_1^C(\eta, \zeta) &= b_1(\eta, \zeta) N_u(\eta, \zeta) \\ B_2^C(\eta, \zeta) &= b_2(\eta, \zeta) N_u(\eta, \zeta)_{,\eta} + b_3(\eta, \zeta) N_u(\eta, \zeta)_{,\zeta} \\ B_3^C(\eta, \zeta) &= b_4(\eta, \zeta) N_u(\eta, \zeta) \end{aligned} \quad (3.15)$$

Based on the virtual work principle [54], a series of theoretical derivations is implemented, and then the governing equation in terms of displacement without external load for 3D SBFEM can be expressed as

$$E_0 \xi^2 u(\xi)_{,\xi\xi} + (2E_0 + E_1^T - E_1) \xi u(\xi)_{,\xi} + (E_1^T - E_2) u(\xi) = 0 \quad (3.16)$$

where, E_i ($i=0, 1, 2$) are coefficient matrices that depend on the geometry and the material properties of the subdomain defined as follows:

$$\begin{aligned} E_0 &= \int_{-1}^{+1} [B_1^C]^T D_e [B_1^C] |J(s)| ds \\ E_1 &= \int_{-1}^{+1} [B_2^C + B_3^C]^T D_e [B_1^C] |J(s)| ds \\ E_2 &= \int_{-1}^{+1} [B_2^C + B_3^C]^T D_e [B_2^C + B_3^C] |J(s)| ds \end{aligned} \quad (3.17)$$

In the formula, $|J(s)|$ represents the Jacobian matrix determinant, and by the introduced vector $X(\xi)$, Eq. (3.16) can be transformed into a system of first-order ordinary differential equations

$$\xi X(\xi)_{,\xi} = -ZX(\xi) \quad (3.18)$$

$$X(\xi) = \begin{bmatrix} u^{0.5}(\xi) \\ q^{-0.5}(\xi) \end{bmatrix} \quad (3.19)$$

where, $q(\xi)$ is the internal nodal force vector, the Hamilton matrix Z is expressed as

$$Z = \begin{bmatrix} E_0^{-1}E_1^T - 0.5I & -E_0^{-1} \\ -E_2 + E_1E_0^{-1}E_1^T & -(E_1E_0^{-1} - 0.5I) \end{bmatrix} \quad (3.20)$$

Eigenvalue decomposition towards coefficient matrix Z is performed to satisfy

$$Z \begin{bmatrix} \psi_u \\ \psi_q \end{bmatrix} = \begin{bmatrix} \psi_u \\ \psi_q \end{bmatrix} S_n \quad (3.21)$$

where, S_n is a diagonal matrix composed of the real parts of the eigenvalues generated from the decomposition of the Z matrix. ψ_u and ψ_q are the modal displacements and forces, respectively. Therefore, the general solutions for the displacements $u(\xi)$ and internal nodal forces $q(\xi)$ of Eq. (3.16) for the polyhedral element are

$$\begin{aligned} u(\xi) &= \psi_u \xi^{-(0.5I+S_n)} c \\ q(\xi) &= \psi_q \xi^{-(0.5I-S_n)} c \end{aligned} \quad (3.22)$$

where, c is an integral constant matrix, which is determined by the node displacement u_b on the subdomain boundary:

$$c = \psi_u^{-1} u_b \quad (3.23)$$

Hence, the SBFEM solution of displacements $u(\xi)$ and nodal internal forces $q(\xi)$ can be obtained by substituting Eq. (3.23) into Eq. (3.22)

$$\begin{aligned} u(\xi) &= \psi_u \xi^{-(0.5I+S_n)} \psi_u^{-1} u_b \\ q(\xi) &= \psi_q \xi^{-(0.5I-S_n)} \psi_u^{-1} u_b \end{aligned} \quad (3.24)$$

Then, the displacement field $u(\xi, \eta, \zeta)$ inside the polyhedral element is obtained by substituting Eq. (3.24) into Eq. (3.2):

$$u(\xi, \eta, \zeta) = N_u(\eta, \zeta) \psi_u \xi^{-(0.5I+S_n)} \psi_u^{-1} u_b \quad (3.25)$$

Therefore, similar to FEM, the polyhedron element shape functions $\Phi(\xi, \eta, \zeta)$ are naturally expressed as:

$$\Phi(\xi, \eta, \zeta) = N_u(\eta, \zeta) \psi_u \xi^{-(0.5I+S_n)} \psi_u^{-1} \quad (3.26)$$

The strain field of a polyhedron element can be derived by substituting Eqs. (3.24) into Eq. (3.14):

$$\begin{aligned} \varepsilon(\xi, \eta, \zeta) &= [B_1^C \psi_u (-S_n - 0.5) \xi^{-(1.5I+S_n)} \psi_u^{-1} + \frac{1}{\xi} B_2^C \psi_u \xi^{-(0.5I+S_n)} \psi_u^{-1} \\ &\quad + B_3^C \psi_u \xi^{-(0.5I+S_n)} \psi_u^{-1}] u_b \end{aligned} \quad (3.27)$$

$$\begin{aligned} B_u^C &= (B_1^C \psi_u (S_n - 0.5) \xi^{-(1.5I+S_n)} \psi_u^{-1}) + \left(\frac{1}{\xi} B_2^C \psi_u \xi^{-(0.5I+S_n)} \psi_u^{-1} \right) \\ &\quad + B_3^C \psi_u \xi^{-(0.5I+S_n)} \psi_u^{-1} \end{aligned} \quad (3.28)$$

According to Hooke's law, the stress field σ is given as

$$\sigma = D_\epsilon \varepsilon \quad (3.29)$$

The stiffness matrix K can be derived from Eq. (3.24) and expressed as

$$K = \psi_q \psi_u^{-1} \quad (3.30)$$

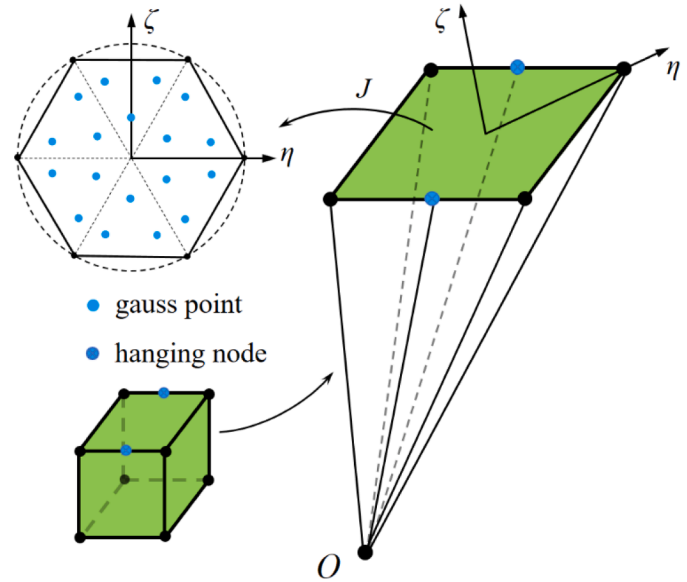


Fig. 6. The diagram of the integral point scheme.

3.4. Integral point scheme

This section introduces the integral scheme for solving SBFEM solutions. For linear problems, only surface element solutions are required. Here, the Hammer integration scheme we adopt is suitable for polygons with an arbitrary number of edges. The conical element, consisting of the surface element with hanging nodes, is taken as an example, as shown in Fig. 6. First, the surface element is mapped to the corresponding canonical element. Then, the canonical element is subdivided into sub-triangular elements, and three integral points are arranged in each sub-triangular element. The selection rules for integral points are the same as those for FEM. In this case, the local coordinates (η, ζ) of the three points are taken as $(1/6, 1/6)$, $(2/3, 1/6)$, and $(1/6, 2/3)$, respectively, and all weights are $1/3$.

4. Numerical examples

In this section, the finite element software program GEODYNA7.0 [55] is used to conduct numerical analysis. This section is divided into three subsections. First, a micro-cantilever beam involving size effects is used to illustrate the high accuracy of the proposed method. Then, a square plate with a circular hole is presented to examine the stress concentration problem. Lastly, an application with complicated geometry is analyzed to demonstrate the capability of the proposed method.

4.1. Verification of high accuracy in size effects

Results from experiments show that the mechanical strength of micro-structures largely depends on their size, known as size effects [56], which cannot be described in classical continuum theory. Therefore, in this section, a micro-cantilever beam is studied to evaluate the accuracy of the proposed method in terms of size effects.

4.1.1. Geometry and material parameters

The micro-cantilever beam is subjected to vertical shear traction of 10 MPa at the free end, and its geometric profile and boundary conditions are depicted in Fig. 7, where $l/h = 8$ and $b/h = 2$. The related material parameters Young's modulus E , Poisson's ratio ν , the two Cosserat parameters shear modulus G_c , and internal length scale $l_c (=l_b = l_t)$ are listed in Table 1.

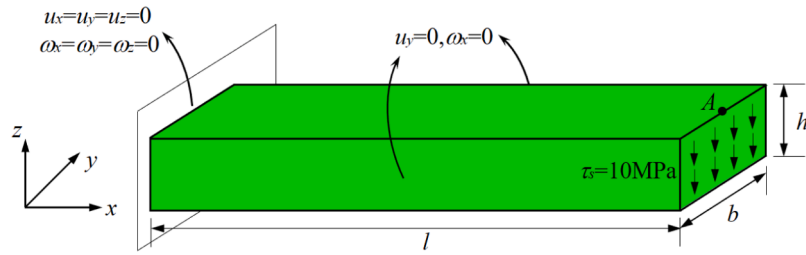


Fig. 7. The geometric profile and boundary conditions of the micro-beam.

Table 1

The material parameters of the micro-cantilever beam.

E/GPa	ν	G_c/GPa	$l_c/\mu\text{m}$
20	0.3	5	250

4.1.2. Mesh discretization

To account for size effects, the micro-beam is proportionally altered in all dimensions, and six different size scenarios are modeled. These scenarios include $h/l_c = 1, 2, 4, 6, 10$, and 20 , respectively. The 3D mesh discretization of the micro-beam is shown in Fig. 8, this results in a total of 400 hexahedral elements with 630 nodes.

4.1.3. Result analysis

According to Timoshenko and Goodier [57], the analytical solution of the deflection of the beam end in classical continuum theory can be expressed as:

$$u_z = \frac{4\tau_s l^3}{Eh^2} (1 - \nu^2) \quad (4.1)$$

All elements in the micro-beam are simulated using the Cosserat SBFEM method, and Table 2 shows the deflection value of point A for different methods. As one can see from Table 2, the analytical solutions of classical continuum theory vary proportionally with the sizes of the structure, thus size effects are not reflected. However, due to the introduction of micro-structure characterized by the internal length scale l_c , solutions of the proposed Cosserat SBFEM method differ significantly from solutions of classical continuum theory. In detail, the smaller the h/l_c ratio is, the greater the difference between the proposed method and the classical continuum solution. Evidently, size effects have been represented.

Table 2 also lists solutions obtained by the high-order Cosserat FEM method in Tang and Hu [14]. It can be seen that the results of the proposed Cosserat SBFEM method are in good agreement with results from the second-order Cosserat FEM method. Therefore, the computational accuracy of the proposed method in size effects can be demonstrated.

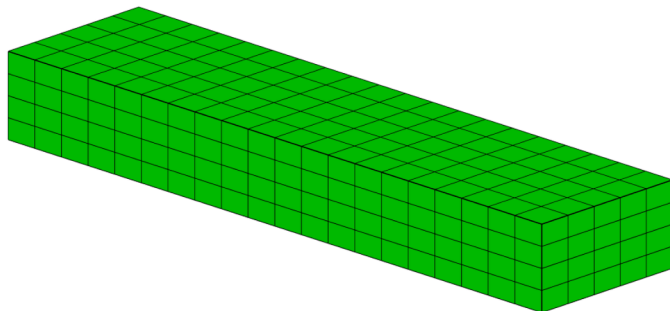


Fig. 8. The 3D mesh of micro-beam.

Table 2

The deflection (μm) of the point A of different methods.

h/l_c	1	2	4	6	10	20
Classical continuum solutions	233.0	465.9	931.8	1397.8	2329.6	4659.2
The proposed method (u^*)	26.3	152.1	607.6	1121.0	2120.0	4501.0
High-order Cosserat FEM (u)	26.4	153.2	616.6	1141.9	2164.2	4596.5
Error (%) / $(100 \times u^* - u /u^*)$	0.38	0.72	1.43	1.86	2.08	2.12

4.2. Analysis of stress concentration problem

4.2.1. Geometry and material parameters

A 3D cube plate containing a circular hole, which is subjected to the uniformly distributed force q on both sides, is considered here to illustrate the stress concentration problem, as illustrated in Fig. 9. The diameter of the circular hole is $2r$, the length of the plate is set to $10r$ to overcome the influence of the boundary on the stress distribution, the height is $10r$ and the thickness is $2r$.

The material parameters of the 3D cube plate are listed in Table 3, in which the Cosserat shear modulus is determined as $G_c/G = 0.5 = c$. To investigate the influence of different internal length scale l_c on stress concentration phenomenon, a set of different l_c/r values are assigned respectively. In addition, a parameter $d = \frac{l_c}{2} \sqrt{\frac{1}{c} + 1}$ is defined.

4.2.2. Mesh discretization

Due to the existence of the hole, maximal stresses, i.e. stress concentration phenomenon, will always emerge around the circular hole. The cube plate is discretized into a refined mesh presented in Fig. 10 to ensure a visually pleasing hole, in which 9088 hexahedron elements

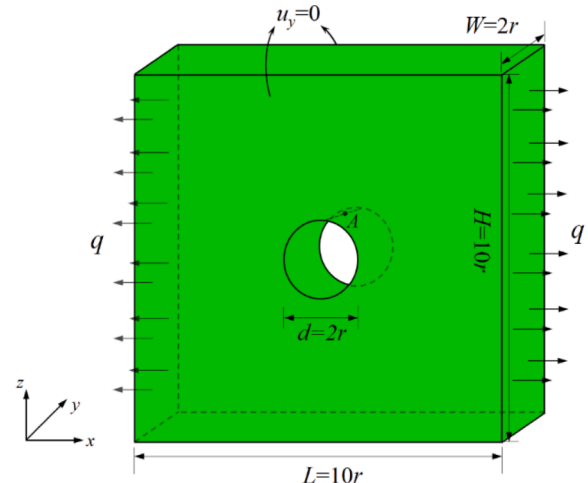


Fig. 9. Geometry of 3D square plate with a circular hole.

Table 3

The material parameters of the micro-cantilever beam.

E/GPa	ν	G_c/GPa	l_c/r
200	0.3	77	0.1, 0.2, 0.3, 0.5, 1.0, 2.0, 4.0

with 15,000 nodes are generated.

4.2.3. Result analysis

The stress concentration factor at the upper edge of the hole along the y -direction, as point A shown in Fig. 9, is defined as

$$K = \frac{\sigma_x}{q} \quad (4.2)$$

where, σ_x is the stress component at point A.

The theoretical solutions for the stress concentration factor around the circular hole with different l_c in 2D conditions can refer to Mindlin [9]. Since only 2D stress concentration solutions are available in the existing literature, for comparison, the 3D analysis is simplified to a plane strain analysis by constraining the y -direction displacements of nodes on the free surface to zero in the model.

Fig. 11 shows the comparisons of the plane strain solutions obtained using the proposed method based on the restricted 3D element mesh and the 2D theoretical solutions derived in Mindlin [9]. It is found that the plane strain solutions based on the proposed method are in good coincidence with the 2D theoretical solutions, which proves that the proposed method has good effectiveness in analyzing stress concentration problems.

Specifically, it can be seen from Fig. 11(a) that with the increase of the internal length scale l_c , the stress concentration factor gradually decreases and tends towards a certain value, which confirms that the internal length scale has the property of weakening the excessive stress concentration phenomenon. Therefore, the internal length scale can accurately capture the effects of large strain gradients and micro-structures.

To further show the function of the proposed method, the stress distribution contour for σ_x of different methods is shown in Fig. 12. As can be seen, the stress distribution profile near the hole obtained from Cosserat SBFEM with $l_c/r=0.1$ is consistent with the SBFEM based on classical continuum theory. Due to the presence of l_c , the high-stress zone on the upper and lower edges of the hole obtained from Cosserat SBFEM is reduced, thereby mitigating the severity of stress concentration.

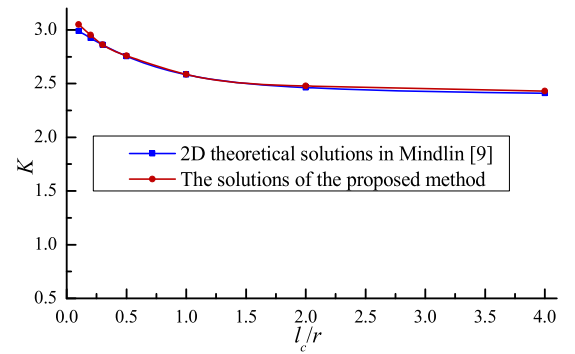
4.2.4. Coupling calculation scheme

It is worth noting that, in Section 4.2.3, the stress concentration only

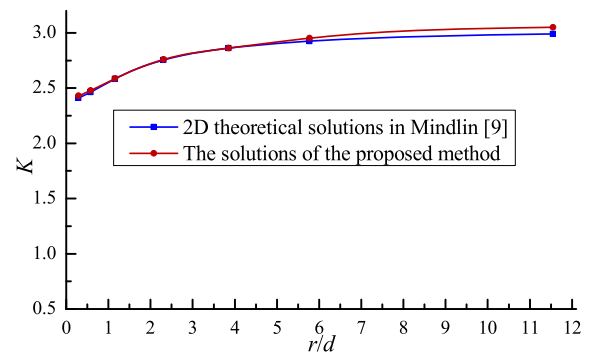
occurs in specific critical zones. Since the number of freedom degrees of the Cosserat element is twice that of the conventional element, this undoubtedly greatly increases the computation cost, and elements in non-stress concentrated regions do not need to be designated as Cosserat continuum. Therefore, a coupling calculation scheme aiming at reducing the computational amount is proposed in this section.

Specifically, the SBFEM analysis is first performed. The calculated cloud contour is shown in Fig. 13, and the stress is mainly concentrated in region B. Then, only elements located in region B are set as Cosserat elements. Therefore, the SBFEM-Cosserat SBFEM coupling program is formed, where the SBFEM elements are calculated using SBFEM, and the Cosserat elements are computed using Cosserat SBFEM.

The comparison of stress distribution σ_x for $l_c/r=0.1$ between

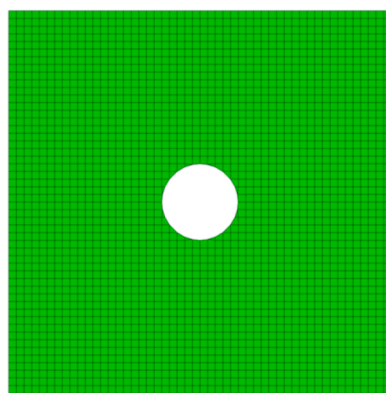


(a) Effect of l_c/r on K

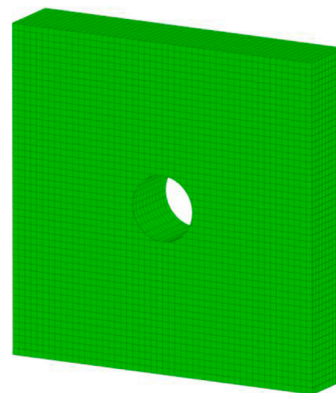


(b) Effect of r/d on K

Fig. 11. The variation curves of stress concentration factor K .



(a) Front view



(b) Side view

Fig. 10. 3D mesh of cube plate with a circular hole.

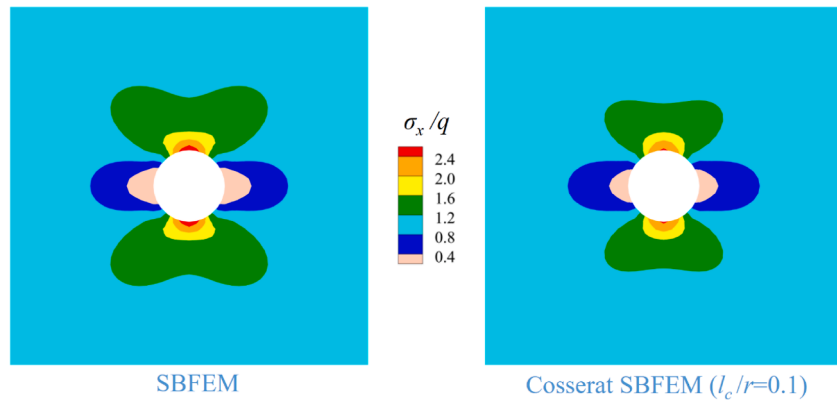


Fig. 12. Cloud contour of stress distribution between different methods.

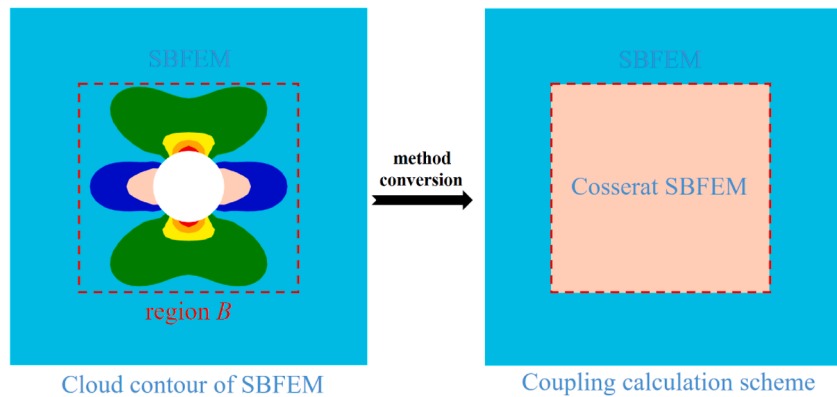


Fig. 13. Schematic diagram of coupling method conversion.

Cosserat SBFEM and the coupling calculation scheme is shown in Fig. 14. As shown in the figure, the obtained distribution rules of different calculation schemes are in good agreement. However, the calculation time of the coupling calculation scheme has improved from 57s to 12s. Therefore, the applied coupling calculation scheme has good performance in reducing calculation costs and ensuring calculation accuracy.

4.3. Application of a complicated structure

In this section, a 3D model of Stanford's Lucy sculpture from the website [58] is selected to verify the adaptability and practicality of the proposed method.

4.3.1. Geometry and material parameters

The sculpture Lucy has dimensions of $102.4 \times 54.1 \times 40.9\text{m}^3$, and its 3D geometry is shown in Fig. 15. The model is fixed at the bottom, and only the self-weight is considered. The material properties of concrete are listed in Table 4.

4.3.2. Mesh discretization

For such a complicated geometric structure, traditional mesh discretization operations will be time-consuming and inefficient. Therefore, this work uses the octree algorithm to automatically generate polyhedral meshes. It recursively divides a hexahedron element into eight equally-sized octants by bisecting the element edges, as shown in Fig. 16. Following this rule, multi-level octree operations can be performed accordingly.

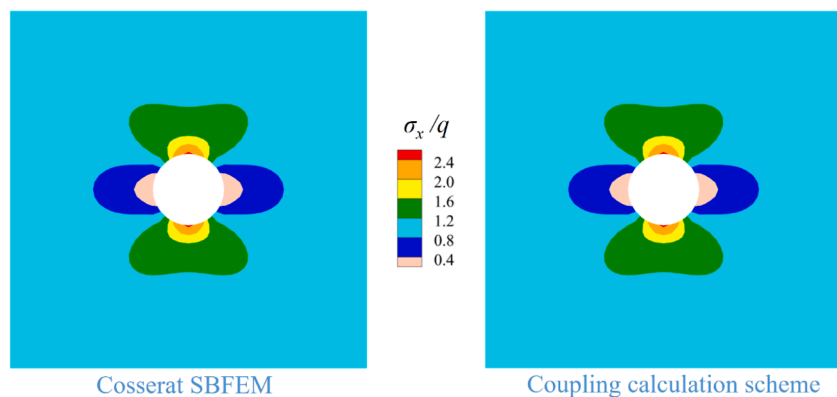


Fig. 14. Comparison of stress distribution between different methods.



Fig. 15. The 3D model of Stanford's Lucy.



Fig. 18. The octree polyhedral mesh for the Lucy model.

Table 4
The material parameters of the Stanford's Lucy.

$\rho/\text{kg}\cdot\text{m}^{-3}$	E/GPa	ν
2350	0.05	0.3

Hanging nodes will appear at the intersection of elements at different levels. The octree algorithm follows a “balance” principle, in which the difference between levels of two adjacent elements is no more than 1, as shown in Fig. 17. Such a balanced strategy simplifies the mesh generation process. The mean-value shape function applied in the proposed

method can be effectively applied to octree meshes with hanging nodes. The discretized polyhedral mesh is shown in Fig. 18, the maximum and minimum element sizes are set as 0.84 m and 0.12 m, respectively. The total discretization process takes only 92s, and this results in a total of 293,517 elements with 379,948 nodes.

The generated mesh indicates that the high curvature zones of the sculpture, such as clothing wrinkles, have been set to a finer mesh with a smaller size, while the mesh size of low curvature zones, such as the front chest and neck, is rough, this ensures an optimal mesh layout for the model. The size transition of the elements within the discretized model is shown in Fig. 19, and the local details of the hanging nodes are displayed.

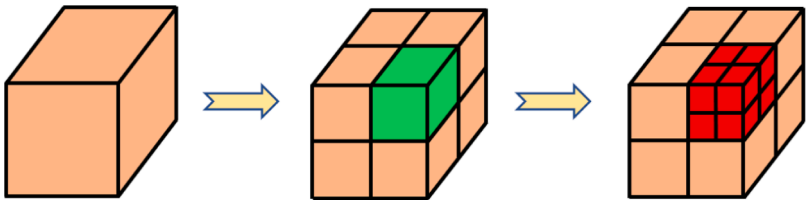


Fig. 16. Octree mesh with three levels.

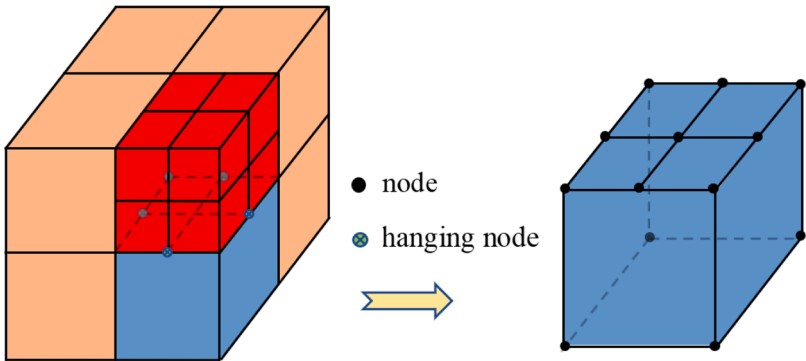


Fig. 17. Balanced strategy of Octree algorithm.

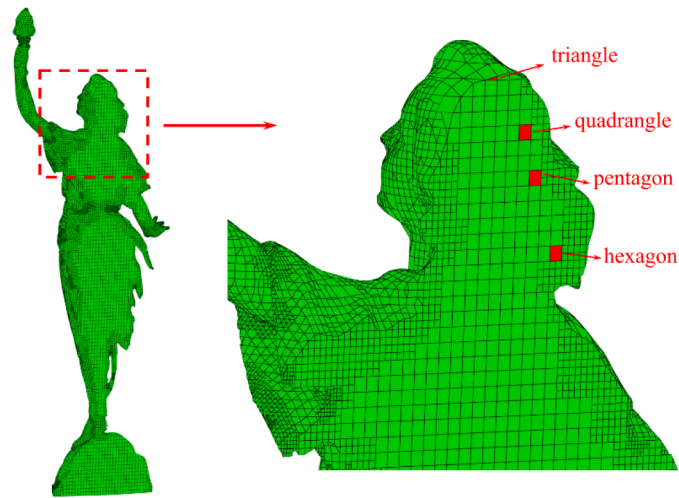


Fig. 19. The detail of transitional element inside the discretized model.

Table 5
Statistical details of different method schemes.

Scheme	Method	Element number	Percent/%
1	FEM	162,236	55.27
	SBFEM	131,281	44.73
2	FEM	143,791	48.99
	SBFEM	111,774	38.08
	Cosserat SBFEM (region I)	37,952	12.93
3	FEM	162,236	42.56
	SBFEM	124,908	55.27
	Cosserat SBFEM (region II)	6373	2.17

4.3.3. Result analysis

To highlight the practicality of the proposed method in the complex model, three calculation schemes, referred to as Schemes 1, 2, and 3 respectively, are applied in this section. Detailed calculation schemes

are provided in Table 5.

4.3.3.1. Scheme 1: FEM-SBFEM coupling. In Scheme 1, for comparison, all elements are first set to be 3D conventional elements based on the classical continuum theory. In the mesh discretization of Fig. 18, two types of elements are used: hexahedron and polyhedron. There are a total of 162,236 hexahedron elements, which make up 55.27% of the total model. Additionally, the octree algorithm generates 131,281 polyhedral elements, accounting for 44.73%. In this manner, the FEM-SBFEM coupling program is adopted, where the hexahedral elements are calculated using FEM, and the polyhedral elements are computed using SBFEM.

The distribution of the maximum principal stress σ_1 on the front of model based on Scheme 1 is shown in Fig. 20. As can be seen, the largest maximum principal stress value occurs on the ankle of model, where the stress concentration phenomenon exists, and the maximum value is 22.8 GPa.

4.3.3.2. Scheme 2: FEM-SBFEM-Cosserat SBFEM (region I) coupling. In this section, the Cosserat method is introduced to evaluate the stress distribution of this model. According to the stress analysis results in Fig. 20, the stress concentration is mainly distributed in a broad area labeled as region I, and all elements in region I are identified as Cosserat elements, as shown in Fig. 21.

In this model, the conventional elements are divided into two categories: 143,791 hexahedral elements and 111,774 polyhedral elements, which constitute 48.99% and 38.08% of the total elements, respectively. Besides, the number of Cosserat elements is 37,952, accounting for 12.93%. The FEM-SBFEM-Cosserat SBFEM coupling program is adopted for Scheme 2. The four-graded aggregate with a maximum particle size of 12 cm has been widely used in the construction of structures world-wide. Therefore, the internal length size, l_c , is set to 0.12 m.

The corresponding numerical simulation is carried out, and the distribution of σ_1 is depicted in Fig. 22(a). As shown in the figure, the stress distribution rule maintains a similarity to the stress distribution based on the classical continuum shown in Fig. 20. However, the area of the stress concentration zone, represented by the red contour, has

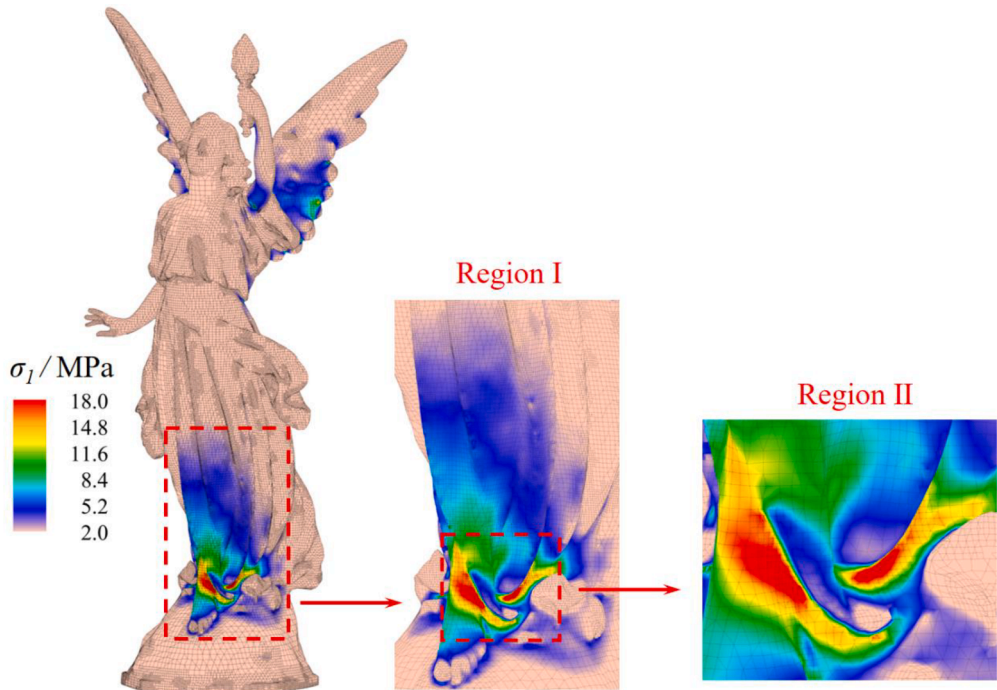


Fig. 20. The distribution of the maximum principal stress σ_1 for Scheme 1.

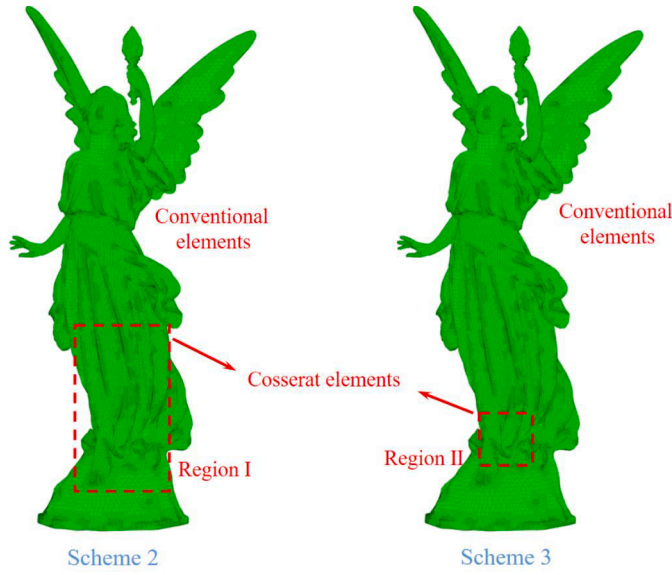


Fig. 21. Elements combinations of different schemes.

decreased. Furthermore, the maximum value of σ_I obtained by Scheme 2 is 18.5 MPa, which represents a 23.24% decrease compared to the classical continuum.

4.3.3.3. Scheme 3: FEM-SBFEM-Cossarat SBFEM (region II) coupling. In Scheme 3, the number of Cossarat elements in Scheme 2 has been further reduced, and only the elements in the highest stress concentration zone called region II in Fig. 20 are arranged as Cossarat elements, and the schematic diagram is shown in Fig. 21(b). The element composition is also listed in Table 5.

The σ_I distribution rule based on Scheme 3 is illustrated in Fig. 22(b). The result is consistent with that in Scheme 2. The extreme value of σ_I analyzed by Scheme 3 is 18.8 MPa, which shows a very small deviation

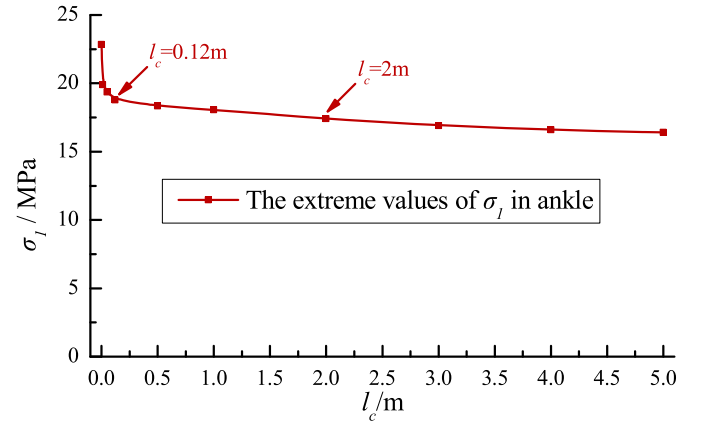


Fig. 23. The extreme values of σ_I with different l_c .

from Scheme 2. Therefore, this improved scheme is also applicable to stress concentration analysis, while significantly reducing computational costs.

Based on the above research, we conclude that the mitigation effect of the micro-structure towards high-stress gradients can be reasonably expressed only by arranging Cossarat elements in the most severe stress concentration zone, which can provide an operational suggestion for related theoretical research.

4.3.4. Sensitivity analysis of l_c

In the research of the Cossarat continuum, the internal length scale l_c with a value of 0.12 m is usually determined empirically, as no relevant theoretical research is available for reference. Therefore, in this section, a sensitivity analysis is conducted to investigate the reasonable range of l_c values in practical engineering.

A series of numerical simulations for different l_c values are performed using Scheme 3. The selected l_c values in the simulations are 0 m, 0.01 m, 0.05 m, 0.12 m, 0.5 m, 1 m, 2 m, 3 m, 4 m, and 5 m, respectively. The

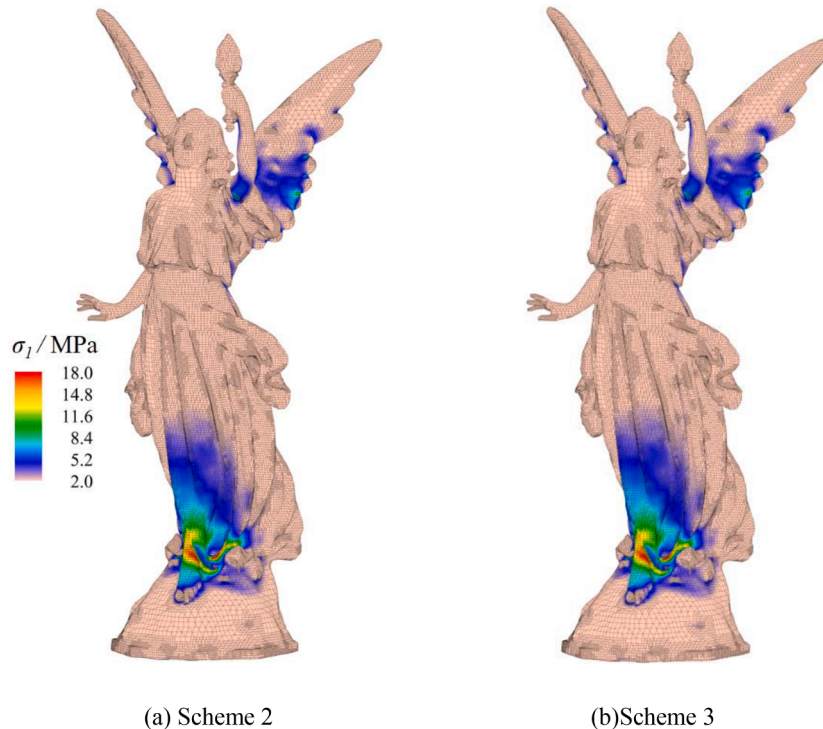


Fig. 22. The distribution of σ_I for different schemes.

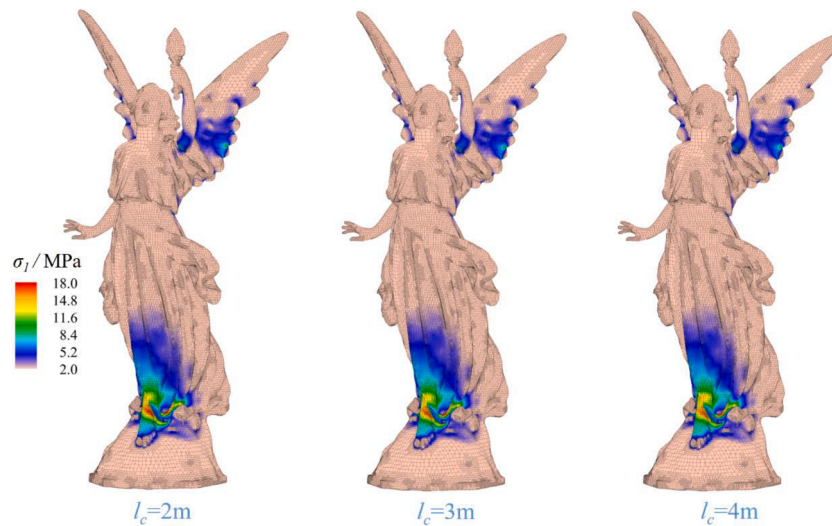


Fig. 24. The distribution of σ_1 with different l_c values.

extreme values of σ_1 in the stress concentration zone corresponding to different l_c are depicted in Fig. 23. As shown in the figure when the value of l_c ranges from 0 to 0.12 m, the extreme value decreases sharply. When the l_c value is in the range of 0.12 to 2 m, the decreasing trend of the extreme values slows down rapidly, with a curve change rate of 0.73. However, when l_c is greater than 2 m, the slope of the curve is only 0.33, and the microscopic effect in this case remains basically unchanged. Fig. 24 exhibits the distribution of σ_1 with different l_c values of 2 m, 3 m, and 4 m, and no significant changes occur in the stress concentration zone.

Based on the above results, we can conclude that $l_c = 0.12$ m is a critical value for determining the micro-structure effect of the Cosserat continuum, this value is sufficient to characterize the micro size effect of the material. Meanwhile, if the stress concentration is particularly severe in a certain region, values within the 0.12–2 m range can also be selected as a substitute.

According to the aforementioned research, it demonstrates that the proposed method can enhance the mesh discretization ability of complex geometric structures. Therefore, the applicability of the proposed method is illustrated.

5. Conclusions

In this paper, a novel and practical formulation of SBFEM for the 3D Cosserat continuum is developed. The semi-analytic technique is employed to construct polyhedral elements through surface discretization. Several numerical analyses are conducted to demonstrate the validity and applicability of the proposed method. The primary conclusions of this study are summarized below:

(1) An excellent accuracy and robustness in terms of size effects is achieved in the proposed method. Benefiting from the characteristics of SBFEM, 3D Cosserat SBFEM solutions maintain good agreement with high-order Cosserat FEM solutions with a maximum error of about 2%. Meanwhile, size effects in the micro-structure have been well characterized by the consideration of the Cosserat continuum.

(2) The stress concentration problems can be effectively weakened by the internal length scale. The Cosserat continuum can demonstrate the stress gradient at the microscale of materials, enabling a more realistic simulation of the stress distribution. More importantly, the proposed method offers a theoretical reference for determining the internal length scale in stress concentration problems, which is of great

value for the design and safety assessment of engineering applications.

(3) The applicability of the Cosserat continuum has been significantly enhanced. The proposed method allows the integration of the octree algorithm into the modeling of complex 3D structures, therefore the application of the Cosserat continuum has been further expanded to the analysis of intricate engineering structures.

The proposed method has the potential to be extended to nonlinear analysis represented by strain localization problems, and its advantages in geotechnical engineering will also be fully utilized, which is also our future research focus.

CRediT authorship contribution statement

Xiupeng Nie: Writing – original draft, Validation, Software, Methodology, Investigation, Formal analysis. **Degao Zou:** Resources, Funding acquisition. **Kai Chen:** Writing – review & editing, Visualization, Supervision, Software, Methodology, Conceptualization. **Jingmao Liu:** Supervision, Software. **Xianjing Kong:** Supervision, Funding acquisition. **Yongqian Qu:** Writing – review & editing.

Declaration of competing interest

The authors declare that they have no known competing financial interests or personal relationships that could have appeared to influence the work reported in this paper.

Data availability

Data will be made available on request.

Acknowledgment

This work was supported by the National Natural Science Foundation of China (Grant Nos. 52192674, 52009018, 52350393).

References

- [1] Tang H, Hu Z, Li X. Three-dimensional pressure-dependent elastoplastic Cosserat continuum model and finite element simulation of strain localization. *Int J Appl Mech* 2013;5(3):1–33. <https://doi.org/10.1142/S1758825113500300>.

- [2] Tang H, Sun F, Zhang Y, Dong Y. Elastoplastic axisymmetric Cosserat continua and modelling of strain localization. *Comput Geotech* 2018;101:159–67. <https://doi.org/10.1016/j.compgeo.2018.05.004>.
- [3] Cosserat E, Cosserat F. *Théorie des corps déformables*. 1909. Paris: A. Hermann et fils.
- [4] Zhu F, Tang H, Zhang X, Li Y, Papazafeiropoulos G. An isogeometric approach to biot-Cosserat continuum for simulating dynamic strain localization in saturated soils. *Comput Geotech* 2021;104036. <https://doi.org/10.1016/j.compgeo.2021.104036>.
- [5] Khoei A, Karimi K. An enriched-FEM model for simulation of localization phenomenon in Cosserat continuum theory. *Comput Mater Sci* 2009;44(2):733–49. <https://doi.org/10.1016/j.commatsci.2008.05.019>.
- [6] Tang H, Wei W, Liu F, Chen G. Elastoplastic Cosserat continuum model considering strength anisotropy and its application to the analysis of slope stability. *Comput Geotech* 2020;117:103235. <https://doi.org/10.1016/j.compgeo.2019.103235>.
- [7] Tang H, Zhu F, Yang D, Papazafeiropoulos G. Numerical simulation of strain localization based on Cosserat continuum theory and isogeometric analysis. *Comput Geotech* 2021;129:103874. <https://doi.org/10.1016/j.compgeo.2020.103874>.
- [8] Toupin R. Elastic materials with couple-stresses. *Arch Ration Mech Anal* 1962;11(1):385–414. <https://doi.org/10.1007/BF00253945>.
- [9] Mindlin R. Influence of couple-stresses on stress concentrations. *Exp. Mech.* 1962;3(1):1–7.
- [10] Borst R. A generalisation of J2-flow theory for polar continua. *Comput Methods Appl Mech Eng* 1993;103(3):347–62. [https://doi.org/10.1016/0045-7825\(93\)90127-J](https://doi.org/10.1016/0045-7825(93)90127-J).
- [11] Providas E, Kattis M. Finite element method in plane Cosserat elasticity. *Comput Struct* 2002;80(27–30):2059–69. [https://doi.org/10.1016/S0045-7949\(02\)00262-6](https://doi.org/10.1016/S0045-7949(02)00262-6).
- [12] Tordesillas A, Peters J, Gardiner B. Shear band evolution and accumulated microstructural development in Cosserat media. *Int J Numer Anal Methods Geomech* 2004;28(10):981–1010. <https://doi.org/10.1002/nag.343>.
- [13] Li X, Tang H. A consistent return mapping algorithm for pressure-dependent elastoplastic Cosserat continua and modeling of strain localization. *Comput Struct* 2005;83(1):1–10. <https://doi.org/10.1016/j.compstruc.2004.08.009>.
- [14] Tang H, Hu Z. Application of the Cosserat continua to numerical studies on the properties of the materials. *Mech Compos Mater* 2016;24(10):797–808. <https://doi.org/10.1080/15376494.2016.1196784>.
- [15] Tang H, Dong Y, Wang T, Dong Y. Simulation of strain localization with discrete element-Cosserat continuum finite element two scale method for granular materials. *J Mech Phys Solids* 2018;122:450–71. <https://doi.org/10.1016/j.jmps.2018.09.029>.
- [16] Riahi A, Curran J. Full 3D finite element Cosserat formulation with application in layered structures. *Appl Math Model* 2009;33(8):3450–64. <https://doi.org/10.1016/j.apm.2008.11.022>.
- [17] Chen K, Zou D, Kong X. A nonlinear approach for the three-dimensional polyhedron scaled boundary finite element method and its verification using Koyana gravity dam. *Soil Dyn Earthq Eng* 2017;96:1–12. <https://doi.org/10.1016/j.soildyn.2017.01.028>.
- [18] Chen K, Zou D, Kong X, Yu X. An efficient nonlinear octree SBFEM and its application to complicated geotechnical structures. *Comput Geotech* 2018;96:226–45. <https://doi.org/10.1016/j.compgeo.2017.10.021>.
- [19] Zou D, Chen K, Kong X, Liu J. An enhanced octree polyhedral scaled boundary finite element method and its applications in structure analysis. *Eng Anal Bound Elem* 2017;84:87–107. <https://doi.org/10.1016/j.enganabound.2017.07.007>.
- [20] Wolf J, Song C. *Finite-element modelling of unbounded media*. Chichester: Wiley; 1996.
- [21] Idelsohn S, Onate E, Calvo N, Pin D. The meshless finite element method. *Int J Numer Methods Eng* 2003;58(6):893–912. <https://doi.org/10.1002/nme.798>.
- [22] Beirão D, Brezzi F, Cangiani A, Manzini G, Marini D, Russo A. Basic principles of virtual element methods. *Math Model Methods Appl Sci* 2013;23(01):199–214. <https://doi.org/10.1142/S0218202512500492>.
- [23] Chen K, Zou D, Kong X, Chan A, Hu Z. A novel nonlinear solution for the polygon scaled boundary finite element method and its application to geotechnical structures. *Comput Geotech* 2017;82:201–10. <https://doi.org/10.1016/j.compgeo.2016.09.013>.
- [24] Chen K, Zou D, Kong X, Zhou Y. Global concurrent cross-scale nonlinear analysis approach of complex CFRD systems considering dynamic impervious panel-rockfill material-foundation interactions. *Soil Dyn Earthq Eng* 2018;114:51–68. <https://doi.org/10.1016/j.soildyn.2018.06.027>.
- [25] Chen K, Zou D, Kong X, Liu J. Elasto-plastic fine-scale damage failure analysis of metro structures based on coupled SBFEM-FEM. *Comput Geotech* 2019;108:280–94. <https://doi.org/10.1016/j.compgeo.2018.12.030>.
- [26] Aladurthi L, Natarajan S, Ooi E, Song C. Scaled boundary finite element method for compressible and nearly incompressible elasticity over arbitrary polytopes. *Int J Numer Methods Eng* 2019;119(13):1379–94. <https://doi.org/10.1002/nme.6095>.
- [27] Song C. Dynamic analysis of unbounded domains by a reduced set of base functions. *Comput Method Appl Mech Eng* 2006;195(33/36):4075–94. <https://doi.org/10.1016/j.cma.2005.07.011>.
- [28] Song C, Ooi E, Natarajan S. A review of the scaled boundary finite element method for two-dimensional linear elastic fracture mechanics. *Eng Fract Mech* 2017;187:45–73. <https://doi.org/10.1016/j.engfracmech.2017.10.016>.
- [29] Song C, Ooi E, Pramod A, Natarajan S. A novel error indicator and an adaptive refinement technique using the scaled boundary finite element method. *Eng Anal Bound Elem* 2018;94:10–24. <https://doi.org/10.1016/j.enganabound.2018.05.010>.
- [30] Song C, Zhang X. High-order composite implicit time integration schemes based on rational approximations for elastodynamics. *Comput Methods Appl Mech Eng* 2024;418:116473. <https://doi.org/10.1016/j.cma.2023.116473>.
- [31] Liu J, Hao C, Ye W, Yang F, Lin G. Free vibration and transient dynamic response of functionally graded sandwich plates with power-law nonhomogeneity by the scaled boundary finite element method. *Comput Methods Appl Mech Eng* 2021;376:113665. <https://doi.org/10.1016/j.cma.2021.113665>.
- [32] Liu J, Hao C, Zhou Y, Ye W. Dynamic analysis of functionally graded sandwich beams using a method named scaled finite element method. *Eng Anal Bound Elem* 2021;130:161–75. <https://doi.org/10.1016/j.enganabound.2021.05.010>.
- [33] Ye W, Zang Q, Liu J, Yang F, Lin G. Three-dimensional bending and free vibration analyses of laminated cylindrical panel with/without elastic foundation using two-dimensional discrete method. *Soil Dyn Earthq Eng* 2023;168:107831. <https://doi.org/10.1016/j.soildyn.2023.107831>.
- [34] Zang Q, Liu J, Ye W, Yang F, Pang R, Lin G. High-performance bending and buckling analyses of cylindrical shells resting on elastic foundation using isogeometric scaled boundary finite element method. *Eur J Mech A-Solid*. 2023;100:105013. <https://doi.org/10.1016/j.euromechsol.2023.105013>.
- [35] Du C, Huang W, Ghaemian M, Jiang S, Zhao Z. New nonlocal multiscale damage model for modelling damage and cracking in quasi-brittle materials. *Eng Fract Mech* 2023;277:108927. <https://doi.org/10.1016/j.engfracmech.2022.108927>.
- [36] Shen X, Du C, Jiang S, Zhang P, Chen L. Multivariate uncertainty analysis of fracture problems through model order reduction accelerated SBFEM. *Appl Math Model* 2024;125:218–40. <https://doi.org/10.1016/j.apm.2023.08.040>.
- [37] Zhang J, Ankit A, Gravenkamp H, Eisentragher S, Song C. A massively parallel explicit solver for elasto-dynamic problems exploiting Octree meshes. *Comput Methods Appl Mech Eng* 2021;380:113811. <https://doi.org/10.1016/j.cma.2021.113811>.
- [38] Zhang J, Zhao M, Eisentragher S, Du X, Song C. An asynchronous parallel explicit solver based on scaled boundary finite element method using octree meshes. *Comput Methods Appl Mech Eng* 2022;401:115653. <https://doi.org/10.1016/j.cma.2022.115653>.
- [39] Zhang G, Zhao M, Zhang J, Du X. Scaled Boundary Perfectly Matched Layer (SBPML): a novel 3D time-domain artificial boundary method for wave problem in general-shaped and heterogeneous infinite domain. *Comput Methods Appl Mech Eng* 2023;403:115738. <https://doi.org/10.1016/j.cma.2022.115738>.
- [40] Zhao M, Liu P, Zhang J, Zhang G, Gao Z, Du X. A direct time-domain FEM-SBFEM-SBPML method for soil-structure interaction analysis using quadtree mesh. *Comput Geotech* 2023;161:105597. <https://doi.org/10.1016/j.compgeo.2023.105597>.
- [41] Zhang W, Li D, Zhang J, Guo X. Minimum length scale control in structural topology optimization based on the Moving Morphable Components (MMC) approach. *Comput Methods Appl Mech Eng* 2016;311:327–55. <https://doi.org/10.1016/j.cma.2016.08.022>.
- [42] Zhang W, Xiao Z, Liu C, Mei Y, Youn S, Guo X. A scaled boundary finite element based explicit topology optimization approach for three-dimensional structures. *Int J Numer Methods Eng* 2020;121(21):4878–900. <https://doi.org/10.1002/nme.6498>.
- [43] Chen K, Zou D, Tang H, Liu J, Zhuo Y. Scaled boundary polygon formula for Cosserat continuum and its verification. *Eng Anal Bound Elem* 2021;126:136–50. <https://doi.org/10.1016/j.enganabound.2021.02.007>.
- [44] Nie X, Chen K, Zou D, Kong X, Liu J, Qu Y. Slope stability analysis based on SBFEM and multistage polytree-based refinement algorithms. *Comput Geotech* 2022;149:104861. <https://doi.org/10.1016/j.compgeo.2022.104861>.
- [45] Qu Y, Eisentragher S, Zhang Z, Zhang L, Song C. Development of a fully automatic damage simulation framework for quasi-brittle materials. *Eng Anal Bound Elem* 2023;157:578–95. <https://doi.org/10.1016/j.enganabound.2023.10.004>.
- [46] Qu Y, Zou D, Kong X, Yu X, Chen K. Seismic cracking evolution for anti-seepage face slabs in concrete faced rockfill dams based on cohesive zone model in explicit SBFEM-FEM frame. *Soil Dyn Earthq Eng* 2020;133:106106.1–106106.14. <https://doi.org/10.1016/j.soildyn.2020.106106>.
- [47] Zhang Z, Liu Y, Dissanayake D, Saputra A, Song C. Nonlocal damage modelling by the scaled boundary finite element method. *Eng Anal Bound Elem* 2019;99:29–45. <https://doi.org/10.1016/j.enganabound.2018.10.006>.
- [48] Zhang Z, Zhou C, Saputra A, Yang Z, Song C. Nonlocal dynamic damage modelling of quasi-brittle composites using the scaled boundary finite element method. *Eng Fract Mech* 2020;240:107362. <https://doi.org/10.1016/j.engfracmech.2020.107362>.
- [49] Yu K, Yang Z, Li H, Ooi E, Li S, Liu G. A mesoscale modelling approach coupling SBFEM, continuous damage phase-field model and discrete cohesive crack model for concrete fracture. *Eng Fract Mech* 2023;278:109030. <https://doi.org/10.1016/j.engfracmech.2022.109030>.
- [50] Zhang G, Zhao M, Du X, Zhang J. Time-domain scaled boundary perfectly matched layer for elastic wave propagation. *Int J Numer Methods Eng* 2023;124(18):3906–34. <https://doi.org/10.1002/nme.7300>.
- [51] Zhang J, Eisentragher S, Zhan Y, Saputra A, Song C. Direct point-cloud-based numerical analysis using Octree meshes. *Comput Struct* 2023;289:107175. <https://doi.org/10.1016/j.compstruc.2023.107175>.
- [52] Huynh H, Zhuang X, Nguyen-Xuan H. A polytree-based adaptive scheme for modeling linear fracture mechanics using a coupled XFEM-SBFEM approach. *Eng Anal Bound Elem* 2020;115:72–85. <https://doi.org/10.1016/j.enganabound.2019.11.001>.
- [53] Floater M, Kós G, Reimers M. Mean value coordinates in 3D. *Comput Aided Geom Dyn* 2005;22(7):623–31. <https://doi.org/10.1016/j.cagd.2005.06.004>.
- [54] Deeks A, Wolf J. A virtual work derivation of the scaled boundary finite-element method for elastostatics. *Comput Mech* 2002;28:489–504. <https://doi.org/10.1007/s00466-002-0314-2>.

- [55] Zou D, Liu J, Chen K, et al. Theoretical introduction and operation instructions of the finite element high performance analysis software system for large geotechnical engineering[R]. Dalian Univ Technol 2018. Press, Dalian.
- [56] Fleck N, Muller G, Ashby M. Strain gradient plasticity: theory and experiment. *Acta Metall Mater* 1994;42(2):475–87. [https://doi.org/10.1016/0956-7151\(94\)90502-9](https://doi.org/10.1016/0956-7151(94)90502-9).
- [57] Timoshenko S, Goodier J. *Theory of elasticity*. McGrawHill; 1970. New York.
- [58] <https://www.thingiverse.com>.